

A Novel Model-Based Estimation Scheme for Battery-Double-Layer Capacitor Hybrid Energy Storage Systems

Satadru Dey¹, *Member, IEEE*, Sara Mohon, *Member, IEEE*, Beshah Ayalew, *Member, IEEE*, Harikesh Arunachalam, *Student Member, IEEE*, and Simona Onori, *Senior Member, IEEE*

Abstract—Battery-double-layer capacitor (DLC) units are becoming popular hybrid energy storage systems (HESS) for vehicle propulsion, auxiliary power units, and renewable energy applications. Safe and optimal operation of the HESS requires real-time monitoring of its constituent subsystems. In this paper, we use a model-based approach to monitor HESS behavior and propose an online combined state and parameter estimation scheme using coupled electrical-thermal dynamical models for each subsystem. In particular, we focus on an HESS composed of a lead-acid (PbA) battery and a DLC for which experiments have been designed to identify the initial model parameters. The estimation scheme uses a novel cascaded observer-based structure which: 1) is designed based on sliding mode methodology and 2) exploits the coupling of the electrical and thermal dynamics. Using Lyapunov's arguments, theoretical conditions are derived which characterize the convergence of the state and parameter estimates in the presence of uncertainties. The effectiveness of the estimation scheme is evaluated via simulation and experimental studies on the PbA battery, the DLC, and the HESS system.

Index Terms—Battery, double-layer capacitors (DLCs), hybrid energy storage system (HESS), sliding mode observers, state and parameter estimation.

I. INTRODUCTION

THE battery-double-layer capacitor (DLC) hybrid energy storage system (HESS) is one kind of HESS that is gaining popularity in various applications. Traditionally, batteries that have been used as auxiliary power units in automobiles and as renewable stationary energy storage have suffered from low power densities. By contrast, DLCs possess high power densities and can offset the load on a battery in peak power situations [1]. Therefore, the combined battery-DLC HESS is appropriate for automotive cold cranking, start/stop, hybrid electric vehicle (HEV) propulsion, and renewable-energy-based microgrids [2], [3].

Manuscript received September 23, 2017; accepted November 26, 2017. Manuscript received in final form December 4, 2017. This work was supported by the U.S. Department of Energy GATE Program under Grant DE-EE0005571. Recommended by Associate Editor L. Wang. (*Corresponding author: Satadru Dey.*)

S. Dey is with the Department of Electrical Engineering, University of Colorado Denver, Denver, CO 80204 USA (e-mail: satadru.dey@ucdenver.edu).

S. Mohon, B. Ayalew, and H. Arunachalam are with the Department of Automotive Engineering, Clemson University, Greenville, SC 29607 USA (e-mail: smohon@clemson.edu; beshah@clemson.edu; harunac@clemson.edu).

S. Onori is with the Department of Energy Resources Engineering, Stanford University, Stanford, CA 94305 USA (e-mail: sonori@stanford.edu).

Color versions of one or more of the figures in this paper are available online at <http://ieeexplore.ieee.org>.

Digital Object Identifier 10.1109/TCST.2017.2781650

The main advantage of using a battery-DLC HESS instead of a traditional battery-only energy storage system is load sharing which can occur between the battery and DLC and can reduce the stress to the battery, thereby prolonging its life [4]. The load sharing of the HESS can either be actively or passively controlled. A passive HESS contains a battery and DLC connected in parallel without a controller. An active HESS contains a passive HESS plus a power electronic device to control the power split between the battery and DLC. Whether passively or actively controlled, real-time monitoring of HESS states and parameters is crucial to guarantee safe, efficient, and optimal operation of the HESS. In this paper, a model-based real-time state and parameter estimation scheme is proposed which can be used for either passive or active battery-DLC HESS. The main focus of this paper involves autostart/autostop application in vehicles which requires high power for a short duration. However, the modeling and estimation approach presented in this paper has the potential to be easily extended to other hybrid applications such as cold cranking an engine and HEV charge sustaining operation.

Important states and parameters for optimizing battery performance and life include state of charge (SOC), internal resistance, and capacity. Internal resistance and capacity, in particular, are useful indicators of battery state of health (SOH) and aging. Existing literature [5]–[7] offers different approaches for online state and parameter estimation of batteries. One group of approaches uses electrochemical models. High computational burden is the major drawback of this approach despite their potentially higher prediction accuracy. This leads to the use of computationally simpler equivalent circuit models (ECMs) for control and estimation purposes. In this paper, we will use an ECM for our estimation scheme. Within ECM, the most often used estimation methods are the Kalman filter (KF)-based approaches such as linear KF, extended KF (EKF), and adaptive EKF [8], [9]. Other than KF-based approaches, ECM-based estimation schemes include nonlinear observers [10], sliding mode observers [11]–[14], and linear parameter varying (LPV) system technique [15]. However, these existing approaches suffer from some drawbacks. For example, the widely used KF-based approaches suffer from: 1) lack of theoretical verification for the estimation error convergence in case of Unscented KF/EKF and 2) highly nontrivial characterization of the noise covariance matrices. Although the other estimation schemes (e.g., sliding mode

observer, nonlinear observer, and LPV-based approaches) generally provide theoretical error convergence proofs, often times they consider isothermal condition. However, the coupling of electrical and thermal dynamics plays a crucial role in predicting the battery behavior.

Similar to batteries, DLCs are sensitive to aging when subjected to abnormal operating conditions [16]. It is necessary to monitor and estimate DLC aging for actively controlled energy management in a battery-DLC HESS [17], [18]. For the DLC, the resistance and capacitances in the ECM represent internal impedance and charge capacity, respectively, and are considered SOH indicators [19]. However, combined state and parameter estimation for DLCs is a less examined topic in the literature than for batteries. In [1] and [20], DLC state estimation was achieved through EKF estimators. In [21] and [22], parameter estimation is studied through least-squares techniques. In [23], offline parameter identification of electrothermal DLC model is explored. However, very few studies consider the real-time combined state and parameter estimation problem. For example, [18] explored such a problem using a dual-KF-based approach. However, the main drawback of these proposed schemes lies in the lack of: 1) theoretical convergence proofs and 2) consideration of electrical–thermal coupling.

In light of the above discussion, this paper proposes an ECM-based estimation scheme for battery-DLC HESS addressing the aforementioned drawbacks. The main contributions of this paper are as follows.

- 1) For battery and DLC estimation, the proposed scheme includes a theoretical verification of combined state and parameter error convergence and considers electrical–thermal coupling.
- 2) The proposed scheme introduces a novel cascaded observer-based framework for combined state and parameter estimation of battery and DLC. This framework exploits the electrical–thermal coupling to decompose the overall estimation problem and simplifies observer design.
- 3) This paper includes the experimentally validated models of the DLC and lead–acid (PbA) battery systems. Furthermore, the effectiveness of the estimation scheme is evaluated using the experimental data.

This paper extends our previously published contribution [24] by: 1) providing convergence proofs with explicit consideration of uncertainties in the model; 2) utilizing experimentally validated battery and DLC models; and 3) verifying the performance of the estimation scheme using the experimental data. The proposed estimation scheme is based on sliding mode observers and equivalent output error injection [25]. Furthermore, the proposed sliding mode-based estimation scheme for batteries differs from the previous sliding mode methods [11]–[14] in that: 1) coupled thermal and electrical dynamics are included and 2) a new cascaded observer-based structure is proposed.

The rest of this paper is organized as follows. Section II briefs the modeling of the HESS elements. Section III describes the proposed estimation scheme. Section IV discusses the identification of a passive battery-DLC HESS,

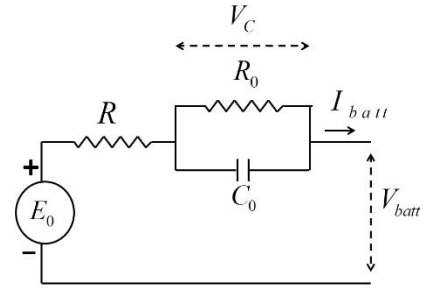


Fig. 1. Battery ECM.

whereas Section V presents simulation and experimental studies. Section VI summarizes the conclusion.

II. HYBRID ENERGY STORAGE SYSTEM MODEL

The HESS under consideration consists of a battery and a DLC. In this section, the modeling of these two energy storage devices is discussed.

A. Battery Model

In this paper, a first-order electrical circuit model (Fig. 1) and a lumped thermal model are utilized for modeling the battery [26].

Using Kirchoff's law and the SOC definition, the electrical dynamics of the battery cell are

$$\dot{V}_c = -\frac{V_c}{R_0 C_0} + \frac{I_{\text{batt}}}{C_0} \quad (1)$$

$$\text{SOC} = -\frac{I_{\text{batt}}}{Q} \quad (2)$$

$$V_{\text{batt}} = E_0 - I_{\text{batt}} R - V_c \quad (3)$$

where V_{batt} is the terminal voltage, I_{batt} is the input current (positive in discharging and negative in charging), R , R_0 , and C_0 are, respectively, the resistors and capacitors of the electrical circuit, V_c is the voltage across the capacitor C_0 , E_0 is the open-circuit potential (OCP), and Q is the capacity of the battery. The battery lumped thermal model [27], [28] is given by

$$m c_{\text{batt}} \dot{T}_{\text{batt}} = I_{\text{batt}}^2 (R + R_0) - h A_{\text{batt}} (T_{\text{batt}} - T_{\text{amb}}) \quad (4)$$

where T_{batt} is the battery cell temperature, $m c_{\text{batt}}$ is the mass times the specific heat capacity of the battery cell, $h A_{\text{batt}}$ is the effective heat transfer coefficient, and T_{amb} is the ambient temperature.

Remark 1: In general, the battery model parameters and the OCP are functions of SOC and T_{batt} . However, for the application considered in this paper, the model parameters are assumed to be fairly constant in a smaller SOC range. The OCP is still a nonlinear function of SOC and battery temperature and can be written as

$$E_0 = f(\text{SOC}, T_{\text{batt}}). \quad (5)$$

B. Double-Layer Capacitor (DLC) Model

Similar to the battery, an electrical circuit model (Fig. 2) with two series resistance–capacitance pairs ($R_d - C_d$ and $R_f - C_f$), and a lumped thermal model is adopted [26] for

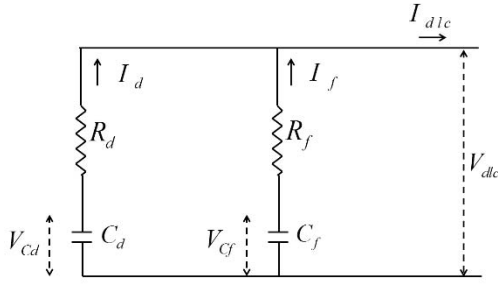


Fig. 2. Electrical ECM of DLC.

the DLC. The $R_d - C_d$ and $R_f - C_f$ branches represent the slower and faster dynamics of DLC, respectively.

The voltage dynamics across the capacitors C_d and C_f can be written as

$$\dot{V}_{cf} = \frac{I_f}{C_f} \quad (6)$$

$$\dot{V}_{cd} = \frac{I_d}{C_d} \quad (7)$$

where V_{cf} is the voltage across the capacitor C_f , V_{cd} is the voltage across the capacitor C_d , I_d is the current flowing through the $R_d - C_d$ branch, and I_f is the current flowing through the $R_f - C_f$ branch. The total current I_{dlc} entering the DLC is given by Kirchoff's current law

$$I_{dlc} = I_f + I_d \quad (8)$$

and the voltage V_{dlc} across the DLC is

$$V_{dlc} = I_f R_f + V_{cf} = I_d R_d + V_{cd} \quad (9)$$

where R_f and R_d are the resistors of the electrical circuit. The lumped thermal dynamics of the DLC are given by

$$mc_{dlc} \dot{T}_{dlc} = I_{dlc}^2 R_f - hA_{dlc}(T_{dlc} - T_{amb}) \quad (10)$$

where T_{dlc} is the DLC temperature, mc_{dlc} is the mass times the specific heat capacity of the DLC, and hA_{dlc} is the effective heat transfer coefficient. The heat generation term in (10) does not include the effect of R_d . This is reasonable because the current through R_d is significantly smaller than the current through R_f as $R_d \gg R_f$. Thus, the effect of R_d on heat generation is neglected [26].

Remark 2: Practically, the DLC model parameters R_f , R_d , C_f , and C_d depend on the SOC, temperature, and current [17]. However, experimental results from [17], and DLC manufacturer's datasheets show that these parameters are mainly functions of temperature while other operating conditions such as current, SOC have negligible effect. Furthermore, the parameter values vary with age although the variation is much slower than the corresponding state dynamics.

Remark 3: The real-time measurements from the HESS are: I_{batt} , T_{batt} , and V_{batt} from the battery and I_{dlc} , T_{dlc} , and V_{dlc} from the DLC.

III. OBSERVER-BASED ESTIMATION SCHEME

In this section, the online estimation scheme for the HESS is described. The estimation scheme consists of a set of sliding

mode observers and open-loop models. In Sections III-A and III-B, the schemes for battery and DLC estimation are discussed individually.

Remark 4: In sliding mode observer design, the observer structure consists of the copy of the plant plus a switching feedback term using available measurement [25]. A sliding manifold has to be defined and if the observer gains are properly designed; the sliding manifold is attained in finite time even in the presence of modeling/parametric uncertainties. Next, we will discuss the basic idea of sliding mode and how a sliding mode observer can be used to estimate an unknown system parameter.

Basic idea of sliding mode observers and equivalent output error injection: for the sake of discussion, consider a scalar first-order linear system

$$\dot{x} = ax + bu \quad (11)$$

where $x \in \mathbb{R}$ is the measured state and hence serves as output, $u \in \mathbb{R}$ is the known input with known bound $|u| \leq \bar{u}$, $a \in \mathbb{R}$ is the known parameter, and $b \in \mathbb{R}$ is the unknown parameter with known upper bound $|b| \leq \bar{b}$. The objective is to estimate the unknown parameter b using a sliding mode observer (the state on the other hand is measured). However, in order to derive the mathematical expression for parameter estimate, we will show the state estimation error convergence as an intermediate step. A sliding mode observer for the system (11) is given by

$$\dot{\hat{x}} = ax + L\text{sgn}(\tilde{x}) \quad (12)$$

where \hat{x} is the estimated state, $\tilde{x} = x - \hat{x}$ is the estimation error, L is the observer gain, and the sliding manifold is $\tilde{x} = 0$. The estimation error dynamics can be written as

$$\dot{\tilde{x}} = bu - L\text{sgn}(\tilde{x}). \quad (13)$$

Considering the Lyapunov function candidate $V = 0.5\tilde{x}^2$, the convergence of the estimation error dynamics can be analyzed by considering the upper bound of the derivative of the Lyapunov function candidate

$$\dot{V} \leq |\tilde{x}|(\bar{b}\bar{u} - L). \quad (14)$$

Under the condition $L > \bar{b}\bar{u}$, then $\dot{V} < \lambda\sqrt{V}$ where $\lambda = \sqrt{2}(\bar{b}\bar{u} - L)$. The solution of the differential inequality (14) is $V(t) \leq (-0.5\lambda t + \sqrt{V(0)})^2$. Hence, the sliding manifold is reached in finite time $t = t^* \leq 2\sqrt{V(0)}/\lambda$ and $\tilde{x} = 0$ and $\dot{\tilde{x}} = 0$. Moreover, the switching term $L\text{sgn}(\tilde{x})$ can be replaced by the so-called equivalent output error injection term [25]. Therefore, we can write from (13)

$$0 = bu - e_{eq} \quad (15)$$

where e_{eq} is the equivalent output error injection term which is a continuous approximation or filtered version of $L\text{sgn}(\tilde{x})$. For implementation purposes, the term e_{eq} is computed by passing $L\text{sgn}(\tilde{x})$ through a low-pass filter as follows:

$$\tau \dot{z} + z = L\text{sgn}(\tilde{x}), \quad z(0) = 0. \quad (16)$$

With a small time constant $\tau > 0$, we have

$$\lim_{\tau \rightarrow 0} z = e_{eq}. \quad (17)$$

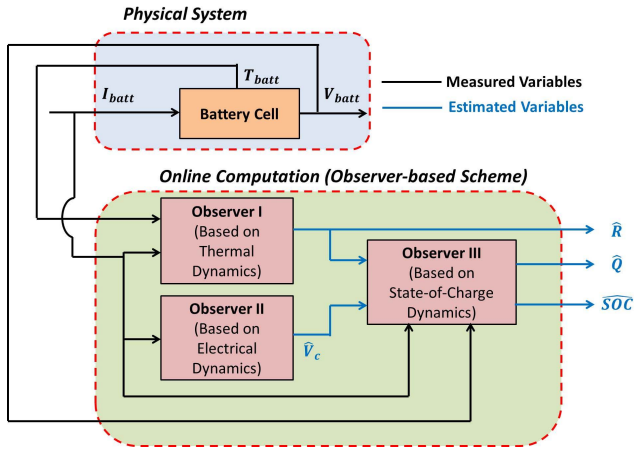


Fig. 3. Online battery state and parameter estimation scheme.

Then, the uncertain parameter b can be estimated as

$$\hat{b} = e_{cq}/u. \quad (18)$$

Remark 5: From the above analysis, two important properties of the sliding mode observer can be noted. First, the estimation error converges to zero in finite time. Second, the equivalent output error injection term can be used to estimate some uncertain model parameters. In this paper, we utilize these two properties for combined state and parameter estimation of the battery and DLC.

A. Combined State and Parameter Estimation of Battery

In this section, we detail the scheme for online estimation of battery states and parameters. The important variables of interest are the SOC, R , and Q . The online estimation scheme, shown in Fig. 3, consists of three observers:

- 1) *Observer I* (based on thermal dynamics);
- 2) *Observer II* (based on the electrical dynamics);
- 3) *Observer III* (based on the SOC dynamics).

Observer I estimates the parameter R using the temperature and current measurements. *Observer II* estimates the electrical state V_c using the open-loop model. *Observer III* estimates the state SOC and parameter Q based on the measured voltage, current, and the estimated R , V_c from *Observer I* and *Observer II*, respectively. SOC of the battery is generally estimated by open-loop coulomb-counting method based on (2). This open-loop approach is prone to error due to the presence of sensor noise and integrator drifting. The OCP is in general a nonlinear function of SOC. In this scheme, we make use of the estimated OCP derived from the estimated states and parameters from *Observer I* and *Observer II*. This OCP, which is a function of SOC, serves as an artificially created nonlinear pseudomeasurement which is then used as the output error injection in the *Observer III*. This estimated OCP essentially helps in creating a closed-loop observer for SOC estimation that can reduce aforementioned effects of uncertainties. While designing the estimation scheme, we make the following assumptions.

Assumption 1: Given Remark 1, the parameters R , R_0 , and C_0 are constant in the range $\text{SOC} \in [\text{SOC}_{\min}, \text{SOC}_{\max}]$ considered for the hybrid application.

Assumption 2: The electrical parameters R_0 and C_0 and the thermal parameters mc_{batt} and hA_{batt} are known with sufficient accuracy. The values for these parameters can be found using offline experimental identification techniques [32].

Remark 6: In the online estimation scheme, we chose to estimate a subset of the total electrical parameters, i.e., $\{R, Q\}$ from the total set $\{R, Q, R_0, C_0\}$. This is due to the fact that the parameters will not be uniquely identifiable if all of them are unknown. On the other hand, the assumption that only a subset is unknown will enable unique identifiability of the parameters. Hence, only a subset of the parameters was chosen to be estimated. However, the choice of the subset is a user-dependent choice. In this particular case, we assumed battery aging influences R and Q the most. One can also assume the parameters $\{Q, R_0, C_0\}$ to be unknown and readily apply the proposed scheme.

Assumption 3: The OCP, E_0 , is a strictly monotonically increasing function of SOC in the range $[\text{SOC}_{\min}, \text{SOC}_{\max}]$ for any given temperature. Note that this assumption is already verified for most of the popular battery chemistries such as PbA, LiCoO₂-Graphite, LiFePO₄-Graphite, and NiMH [29]–[31].

Lemma 1: From Assumption 3, for a given $T_{\text{batt}} = T_{\text{batt}}^*$, given any two points $\text{SOC}^{(1)}$ and $\text{SOC}^{(2)}$ in the SOC domain within the range $\text{SOC} \in [\text{SOC}_{\min}, \text{SOC}_{\max}]$ and their corresponding OCP values, i.e., $E_0^{(1)} = f(\text{SOC}^{(1)}, T_{\text{batt}}^*)$ and $E_0^{(2)} = f(\text{SOC}^{(2)}, T_{\text{batt}}^*)$, the following holds true:

$$\text{sgn}(E_0^{(1)} - E_0^{(2)}) = \text{sgn}(\text{SOC}^{(1)} - \text{SOC}^{(2)}). \quad (19)$$

This can be easily verified from common battery OCP–SOC curves.

The battery dynamics under the presence of uncertainties is given by

$$\dot{V}_c = -\frac{V_c}{R_0 C_0} + \frac{I_{\text{batt}}}{C_0} + \eta_{V_c} \quad (20)$$

$$\dot{\text{SOC}} = -\frac{I_{\text{batt}}}{Q} + \eta_{\text{SOC}} \quad (21)$$

$$V_{\text{batt}} = E_0 - I_{\text{batt}} R - V_c + \eta_V \quad (22)$$

$$mC_{\text{batt}} \dot{T}_{\text{batt}} = I_{\text{batt}}^2 (R + R_0) - hA_{\text{batt}} (T_{\text{batt}} - T_{\text{amb}}) + \eta_{T_b} \quad (23)$$

where η_{V_c} , η_{SOC} , η_V , and η_{T_b} are the modeling uncertainties, which can be state and/or input dependent. In other words, we treat these uncertainties as bounded, unknown, exogenous (and possibly time varying) inputs acting on the nominal battery model.

Assumption 4: The uncertainties η_i , $i \in \{V_c, \text{SOC}, V, T_b\}$ and their time derivatives $\dot{\eta}_i$ are assumed to be bounded by known finite values $|\eta_i| \leq \eta_{i \max}$ and $|\dot{\eta}_i| \leq \dot{\eta}_{i \max}$.

Remark 7: The physical origins of η_i are as follows:

- 1) state and possibly input dependence of the model parameters;
- 2) unmodeled dynamics that arise under high current scenarios;

- 3) parametric uncertainties arising due to manufacturing variability;
- 4) parametric variations due to degradation.

Due to these many possible sources, it is difficult to achieve a complete and scalable characterization of η_i . Hence, we resort to this simple representation where the uncertainties are modeled as additive time-varying exogenous disturbances. Although simple, it still provides us an idea how the state and/or parameter estimates are ‘‘corrupted’’ by the presence of such uncertainties. Specifically, it helps us to benchmark the upper bound of the state/parameter estimation errors, in terms of upper bounds of η_i . Furthermore, all possible aforementioned sources of η_i are physical. For example, the functions that capture the parameter dependence are bounded under bounded temperature, SOC and current (as found in [26]). Furthermore, the outcomes of the unmodeled dynamics, for example, electrolyte dynamics in batteries, are always finite. Hence, Assumption 4 is justified.

Now, the *Observers I–III* for the battery state-parameter estimation are given as follows:

Observer I:

$$m c_{\text{batt}} \dot{\tilde{T}}_{\text{batt}} = I_{\text{batt}}^2 R_0 - h A_{\text{batt}} (\hat{T}_{\text{batt}} - T_{\text{amb}}) + L_T \text{sgn}(\tilde{T}_{\text{batt}}) \quad (24)$$

$$\hat{R} = v_T / I_{\text{batt}}^2 \quad (25)$$

where v_T is the equivalent output error injection which is a continuous approximation or filtered version of $L_T \text{sgn}(\tilde{T}_{\text{batt}})$.

Observer II:

$$\dot{\hat{V}}_c = -\frac{\hat{V}_c}{R_0 C_0} + \frac{I_{\text{batt}}}{C_0} \quad (26)$$

Observer III:

$$\dot{\widehat{\text{SOC}}} = L_{\text{SOC}} \text{sgn}(V_{\text{batt}} + I_{\text{batt}} \hat{R} + \hat{V}_c - \hat{E}_0) \quad (27)$$

$$\hat{Q} = I_{\text{batt}} / v_{\text{SOC}} \quad (28)$$

where v_{SOC} is the equivalent output error injection which is a continuous approximation or filtered version of $L_{\text{SOC}} \text{sgn}(V_{\text{batt}} + I_{\text{batt}} \hat{R} + \hat{V}_c - \hat{E}_0)$; \hat{T}_{batt} , \hat{R} , \hat{V}_c , $\widehat{\text{SOC}}$, and \hat{Q} denote the estimates of the corresponding states and parameters; $\hat{E}_0 = f(\widehat{\text{SOC}}, T_{\text{batt}})$; $\tilde{T}_{\text{batt}} = T_{\text{batt}} - \hat{T}_{\text{batt}}$ and L_T , $L_{\text{SOC}} > 0$ are constant observer gains to be selected.

Furthermore, other estimation errors are defined as: $\tilde{E}_0 = E_0 - \hat{E}_0$, $\widehat{\text{SOC}} = \text{SOC} - \widehat{\text{SOC}}$, $\tilde{V}_c = V_c - \hat{V}_c$, $\tilde{R} = R - \hat{R}$, $\tilde{Q} = Q - \hat{Q}$.

Theorem 1: Consider the system dynamics (20)–(23) and the observer structure (24)–(28). If Assumptions 1–4 and Lemma 1 hold true, then, the estimation errors \tilde{R} , \tilde{V}_c , $\widehat{\text{SOC}}$, and \tilde{Q} converge to bounded values in their respective error space in finite time, if the observer gains satisfy the following conditions:

$$L_T > |I_{\text{batt}}^2 R|_{\text{max}} + \eta_{T_b \text{max}} \quad (29)$$

$$L_{\text{SOC}} > \left| \frac{I_{\text{batt}}}{Q} \right|_{\text{max}} + \eta_{\text{SOC-max}} + \dot{\eta}_{S\text{-comb1-max}} \quad (30)$$

where $\eta_{S\text{-comb1-max}}$ is the combined effect of the uncertainties defined in the proof.

Proof: First, we analyze *Observer I* which is based on the thermal dynamics. Note that the objective of the *Observer I* is to estimate the unknown parameter R , not to estimate the already measured temperature state T_{batt} . However, we show convergence proof of the state estimation error \tilde{T}_{batt} as an intermediate step to the convergence proof for the parameter error (\tilde{R}). Subtracting (24) from (23), the error dynamics of the *Observer I* can be written as

$$m c_{\text{batt}} \dot{\tilde{T}}_{\text{batt}} = I_{\text{batt}}^2 R - h A_{\text{batt}} \tilde{T}_{\text{batt}} + \eta_{T_b} - L_T \text{sgn}(\tilde{T}_{\text{batt}}). \quad (31)$$

Note that the sliding manifold in this case is $s_T = \tilde{T}_{\text{batt}} = 0$ as \tilde{T}_{batt} is inside the sign function. The error dynamics can be analyzed by choosing the positive definite the Lyapunov function candidate $V_T = 0.5 m c_{\text{batt}} \tilde{T}_{\text{batt}}^2$. The derivative of the Lyapunov function candidate can be written as

$$\dot{V}_T = m c_{\text{batt}} \tilde{T}_{\text{batt}} \dot{\tilde{T}}_{\text{batt}} \quad (32)$$

$$\Rightarrow \dot{V}_T = I_{\text{batt}}^2 R \tilde{T}_{\text{batt}} - h A_{\text{batt}} \tilde{T}_{\text{batt}}^2 + \eta_{T_b} \tilde{T}_{\text{batt}} - L_T \tilde{T}_{\text{batt}} \text{sgn}(\tilde{T}_{\text{batt}}). \quad (33)$$

Applying the inequality $mn \leq |mn| \leq |m||n| \leq |m|_{\text{max}}|n|_{\text{max}}$ on the first and third terms of (33), and considering the fact that $h A_{\text{batt}} \tilde{T}_{\text{batt}}^2 > 0$, we can write the upper bound of \dot{V}_T as

$$\dot{V}_T \leq |\tilde{T}_{\text{batt}}| \{ |I_{\text{batt}}^2 R|_{\text{max}} + |\eta_{T_b}|_{\text{max}} - L_T \} \quad (34)$$

$$\Rightarrow \dot{V}_T \leq -\alpha \sqrt{V_T} \quad (35)$$

where $\alpha = -((|I_{\text{batt}}^2 R|_{\text{max}} + \eta_{T_b \text{max}} - L_T) / \sqrt{0.5 m c_{\text{batt}}})$. If the observer gain satisfies the condition $L_T > |I_{\text{batt}}^2 R|_{\text{max}} + \eta_{T_b \text{max}}$, then we have $\alpha > 0$ and hence, the solution of the differential inequality (35) can be written as

$$V_T(t) \leq \left\{ -\frac{\alpha}{2} t + \sqrt{V_T(t_0)} \right\}^2. \quad (36)$$

It can be concluded from the above analysis that the sliding manifold $s_T = \tilde{T}_{\text{batt}} = 0$ can be attained in finite time provided the observer gain satisfies the condition $L_T > |I_{\text{batt}}^2 R|_{\text{max}} + \eta_{T_b \text{max}}$. The $|I_{\text{batt}}^2 R|_{\text{max}}$ value can be known from the specific battery characteristics and operating input current ranges. The finite time is mainly determined by the magnitudes of the $V_T(t_0)$, the magnitude of $|I_{\text{batt}}^2 R|$ and the observer gain L_T . At the sliding manifold, $s_T = \tilde{T}_{\text{batt}} = 0$ and $\dot{s}_T = \dot{\tilde{T}}_{\text{batt}} = 0$ and (31) can be written as

$$0 = I_{\text{batt}}^2 R + \eta_{T_b} - v_T \quad (37)$$

where v_T is the equivalent output error injection signal required to maintain the sliding motion and essentially a continuous approximation (filtered version) of the switching term $L_T \text{sgn}(\tilde{T}_{\text{batt}})$. In practical implementation, v_T can be extracted from the sliding mode observer by passing the switching signal $L_T \text{sgn}(\tilde{T})$ through a low-pass filter with unity steady-state gain. Furthermore, from (25) and (37), we can write

$$\hat{R} = \frac{v_T}{I_{\text{batt}}^2} = \frac{I_{\text{batt}}^2 R + \eta_{T_b}}{I_{\text{batt}}^2} = R + \frac{\eta_{T_b}}{I_{\text{batt}}^2}. \quad (38)$$

From (38), it can be concluded that the estimation error \tilde{R} converges in finite time to a bounded region determined

by $(\eta_{T_b}/I_{\text{batt}}^2)$. Next, subtracting (26) from (20), the estimation error for *Observer II* can be written as

$$\dot{\tilde{V}}_c = -\frac{\tilde{V}_c}{R_0 C_0} + \eta_{V_c}. \quad (39)$$

Following similar steps as before, with the Lyapunov function candidate $V_{LC} = 0.5\tilde{V}_c^2$, we can conclude that $\dot{V}_{LC} < 0$ under the condition $|\tilde{V}_c| > \eta_{V_c \max} R_0 C_0$, however, $\dot{V}_{LC} > 0$ when $|\tilde{V}_c| < \eta_{V_c \max} R_0 C_0$. Therefore, it can be concluded from the above analysis that the estimation error \tilde{V}_c converges to a bounded value determined by the magnitude $\eta_{V_c \max} R_0 C_0$ in some finite time.

As the estimation errors \tilde{R} and \tilde{V}_c converge to bounded values in their respective error space, we can write

$$\begin{aligned} V_{\text{batt}} + I_{\text{batt}} \hat{R} + \hat{V}_c &\rightarrow V_{\text{batt}} + I_{\text{batt}} R + V_c + \eta_{\text{comb1}} \\ &= E_0 + \eta_{\text{comb1}} \end{aligned} \quad (40)$$

where η_{comb1} is the combined effect of the uncertainties in \tilde{R} , \tilde{V}_c , and η_V . Furthermore, using Lemma 1, the following can be written:

$$\text{sgn}(\tilde{E}_0 + \eta_{\text{comb1}}) = \text{sgn}(\widetilde{\text{SOC}} + \eta_{S\text{-comb1}}) \quad (41)$$

where $\tilde{E}_0 = E_0 - \hat{E}_0$ and $\eta_{S\text{-comb1}}$ is the equivalent uncertainty in $\widetilde{\text{SOC}}$ error space due to the effect of η_{comb1} in \tilde{E}_0 error space. Now, subtracting (27) from (21), and considering (41), the estimation error dynamics for *Observer III* can be written as

$$\dot{\widetilde{\text{SOC}}} = -\frac{I_{\text{batt}}}{Q} + \eta_{\text{SOC}} - L_{\text{SOC}} \text{sgn}(\widetilde{\text{SOC}} + \eta_{S\text{-comb1}}). \quad (42)$$

Analyzing the error dynamics (42) with the Lyapunov function candidate $V_{\text{SOC}} = 0.5s_{\text{SOC}}^2$, it can be concluded that the sliding manifold $s_{\text{SOC}} = \widetilde{\text{SOC}} + \eta_{S\text{-comb1}} = 0$ can be attained in some finite time, by selecting the observer gain $L_{\text{SOC}} > |(I_{\text{batt}}/Q)|_{\max} + \eta_{\text{SOC}\text{-max}} + \dot{\eta}_{S\text{-comb1}\text{-max}}$. The value of $|I/Q|_{\max}$ can be known from the specific battery characteristics and reasonable input current range. At the sliding manifold, we have $s_{\text{SOC}} = \widetilde{\text{SOC}} + \eta_{S\text{-comb1}} = 0$ and $\dot{s}_{\text{SOC}} = \dot{\widetilde{\text{SOC}}} + \dot{\eta}_{S\text{-comb1}} = 0$. Therefore, $\widetilde{\text{SOC}}$ converges to a bounded value determined by $\eta_{S\text{-comb1}}$ in finite time. Furthermore, considering $\dot{s}_{\text{SOC}} = \dot{\widetilde{\text{SOC}}} + \dot{\eta}_{S\text{-comb1}} = 0$, (42) can be written as

$$-\dot{\eta}_{S\text{-comb1}} = -\frac{I_{\text{batt}}}{Q} + \eta_{\text{SOC}} - v_{\text{SOC}} \quad (43)$$

where v_{SOC} is the equivalent output error injection. Furthermore, from (43) and (28), the following can be written as:

$$\frac{1}{\hat{Q}} = \frac{v_{\text{SOC}}}{I_{\text{batt}}} = \frac{1}{Q} + \frac{\eta_{\text{SOC}} + \dot{\eta}_{S\text{-comb1}}}{I_{\text{batt}}}. \quad (44)$$

Defining $Q_{\text{inv}} = 1/Q$, $\hat{Q}_{\text{inv}} = 1/\hat{Q}$, and $\tilde{Q}_{\text{inv}} = Q_{\text{inv}} - \hat{Q}_{\text{inv}}$, we can write

$$\tilde{Q}_{\text{inv}} = \frac{\eta_{\text{SOC}} + \dot{\eta}_{S\text{-comb1}}}{I_{\text{batt}}}. \quad (45)$$

Therefore, it can be concluded that the estimation error \tilde{Q}_{inv} , and hence \tilde{Q} will converge to a bounded region determined by the magnitude of $(\eta_{\text{SOC}} + \dot{\eta}_{S\text{-comb1}})/I_{\text{batt}}$ in some finite time.

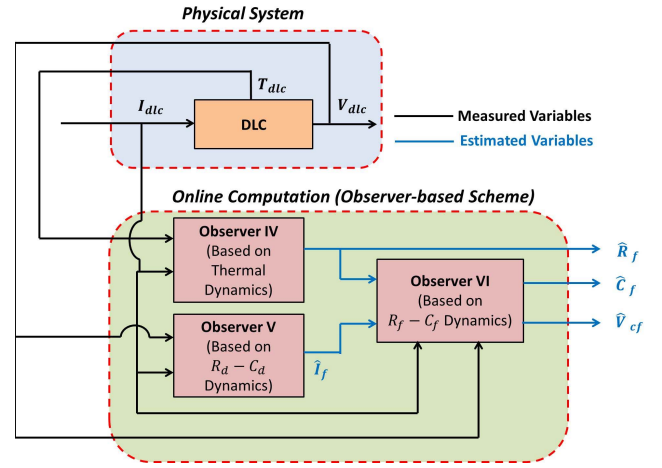


Fig. 4. Online DLC state and parameter estimation scheme.

B. Combined State and Parameter Estimation of DLC

In this section, we discuss the design of online estimation of state and parameters of the DLC. As discussed before, V_{cd} and V_{cf} represents the slow and fast dynamics of the DLC, respectively. In the estimation scheme, we focus on the V_{cf} dynamics and estimate the variables associated with $R_f - C_f$ branch of the DLC, namely, the state V_{cf} and parameters R_f and C_f . The schematic of the DLC online estimation scheme is shown in Fig. 4.

The estimation scheme consists of three observers:

- 1) *Observer IV* (based on the DLC thermal dynamics);
- 2) *Observer V* (based on the $R_d - C_d$ dynamics);
- 3) *Observer VI* (based on the $R_f - C_f$ dynamics).

Observer IV estimates the temperature T_{dlc} and the parameter R_f using the temperature and current measurements. *Observer V* estimates the current through the $R_d - C_d$ electrical branch. *Observer VI* estimates the state V_{cf} and parameter C_f based on the measurement V_{dlc} , I_{dlc} and the estimated \hat{R}_f and \hat{i}_f from *Observer IV* and *Observer V*, respectively. Next, we make the following assumptions.

Assumption 5: From Remark 2, the parameters R_f , R_d , C_f , and C_d are functions of temperature. Since the thermal dynamics is much slower than that of the electrical dynamics, these parameters can be assumed to change much slower than the electrical states.

Assumption 6: The parameters R_d and C_d , along with the thermal parameters mc_{dlc} and hA_{dlc} are known with sufficient accuracy. The values for these parameters can be found by experimental offline identification techniques. Similar to the battery estimation, we chose to estimate a subset of the electrical parameters, i.e., $\{R_f, C_f\}$ from the total set $\{R_d, C_d, R_f, C_f\}$ to enable unique identifiability of the parameters. One can also choose the parameters $\{R_d, C_d\}$ to be unknown and readily apply the proposed scheme with minor technical modification.

The DLC dynamics under the presence of uncertainties is given by

$$\dot{V}_{\text{cf}} = \frac{I_f}{C_f} + \eta_f \quad (46)$$

$$\dot{V}_{cd} = \frac{I_d}{C_d} + \eta_d \quad (47)$$

$$I_{dlc} = I_f + I_d \quad (48)$$

$$V_{dlc} = I_f R_f + V_{cf} + \eta_{V2} = I_d R_d + V_{cd} + \eta_{V2} \quad (49)$$

$$mc_{dlc} \dot{\tilde{T}}_{dlc} = I_{dlc}^2 R_f - hA_{dlc}(T_{dlc} - T_{amb}) + \eta_{T_D} \quad (50)$$

where η_f , η_d , η_{V2} , and η_{T_D} are the modeling uncertainties, which can be state and/or input dependent. In the following analysis, we treat these uncertainties as bounded, unknown, exogenous (and possibly time varying) inputs acting on the nominal DLC model.

Assumption 7: The uncertainties and their time derivatives are assumed to be bounded by known finite values $|\eta_i| \leq \eta_{i-\max}$ and $|\dot{\eta}_i| \leq \dot{\eta}_{i-\max}$ where $i \in \{f, d, V_2, T_D\}$.

Now, the observers for the DLC state and parameter estimation are given as follows:

Observer IV:

$$mc_{dlc} \dot{\tilde{T}}_{dlc} = -hA_{dlc}(\tilde{T}_{dlc} - T_{amb}) + L_{T2} \text{sgn}(\tilde{T}_{dlc}) \quad (51)$$

$$\hat{R}_f = v_{T2}/I_{dlc}^2 \quad (52)$$

where v_{T2} is the equivalent output error injection which is a continuous approximation or filtered version of $L_{T2} \text{sgn}(\tilde{T}_{dlc})$.

Observer V:

$$\dot{\hat{V}}_{cd} = \left(\frac{V_{dlc} - \hat{V}_{cd}}{R_d} \right) \frac{1}{C_d} \quad (53)$$

$$\hat{I}_d = \frac{V_{dlc} - \hat{V}_{cd}}{R_d} \quad (54)$$

Observer VI:

$$\dot{\hat{V}}_{cf} = L_V \text{sgn}(V_{dlc} - \hat{I}_f \hat{R}_f - \hat{V}_{cf}) \quad (55)$$

$$\hat{C}_f = \hat{I}_f / v_V \quad (56)$$

where v_V is the equivalent output error injection which is a continuous approximation or filtered version of $L_V \text{sgn}(\tilde{V}_{cf})$; \hat{T}_{dlc} , \hat{R}_f , \hat{R}_d , \hat{V}_{cf} , \hat{V}_{cd} , \hat{I}_d and \hat{C}_f denote the estimates of the corresponding states and parameters; $\hat{I}_f = I_{dlc} - \hat{I}_d$; $\tilde{T}_{dlc} = T_{dlc} - \hat{T}_{dlc}$ and $L_V > 0$ and $L_{T2} > 0$ are constant observer gains. Furthermore, other estimation errors are defined as: $\tilde{V}_{cf} = V_{cf} - \hat{V}_{cf}$, $\tilde{R}_f = R_f - \hat{R}_f$, $\tilde{V}_{cd} = V_{cd} - \hat{V}_{cd}$, $\tilde{I}_d = I_d - \hat{I}_d$, $\tilde{C}_f = C_f - \hat{C}_f$, and $\tilde{C}_d = C_d - \hat{C}_d$.

Theorem 2: Given the DLC system dynamics (46)–(50) and the observer (51)–(56), and assuming Assumptions 5–7 hold true, then the estimation errors \tilde{R}_f , \tilde{V}_{cd} , \tilde{I}_f , \tilde{V}_{cf} , and \tilde{C}_f converge to bounded values in respective error space in finite time if the observer gains satisfy the following conditions:

$$L_{T2} > |I_{dlc}^2 R_f|_{\max} + \eta_{T_{D-\max}} \dot{\hat{V}}_{cf} \\ = L_V \text{sgn}(V_{dlc} - \hat{I}_f \hat{R}_f - \hat{V}_{cf}) \quad (57)$$

$$L_V > |I_f / C_f|_{\max} + \eta_{f-\max} \quad (58)$$

Proof: Subtracting (51) from (50), the error dynamics for *Observer I* can be written as

$$mc_{dlc} \dot{\tilde{T}}_{dlc} = I_{dlc}^2 R_f + \eta_{T_D} - hA_{dlc} \tilde{T}_{dlc} - L_{T2} \text{sgn}(\tilde{T}_{dlc}). \quad (59)$$

Following similar steps as shown in Theorem 1, and choosing a Lyapunov function candidate $V_{T2} = 0.5mc_{dlc} \tilde{T}_{dlc}^2$, we can conclude that the sliding manifold $s_{T2} = \dot{\tilde{T}}_{dlc} = 0$ can

be attained in finite time given the observer gain $L_{T2} > |I_{dlc}^2 R_f|_{\max} + \eta_{T_{D-\max}}$. At the sliding manifold, we have $s_{T2} = \dot{\tilde{T}}_{dlc} = 0$ and $\dot{s}_{T2} = \ddot{\tilde{T}}_{dlc} = 0$ and (59) can be written as

$$0 = I_{dlc}^2 R_f + \eta_{T_D} - v_{T2} \quad (60)$$

where v_{T2} is the equivalent output error injection signal. Furthermore, from (60) and (52), we can write

$$\hat{R}_f = \frac{v_{T2}}{I_{dlc}^2} = \frac{I_{dlc}^2 R_f + \eta_{T_D}}{I_{dlc}^2} = R_f + \frac{\eta_{T_D}}{I_{dlc}^2}. \quad (61)$$

This concludes that the estimation error \tilde{R}_f converges to a bounded value of (η_{T_D}/I_{dlc}^2) . Next, the estimation error for *Observer V* is written as

$$\dot{\tilde{V}}_{cd} = -\frac{\tilde{V}_{cd} + \eta_{V2}}{R_d C_d} + \eta_d. \quad (62)$$

Again, utilizing the Lyapunov function candidate $V_{LD} = 0.5\tilde{V}_{cd}^2$, we can conclude that the estimation error \tilde{V}_{cd} will converge to a bounded value determined by the magnitude $\eta_{d-\max} R_d C_d$ in some finite time. Therefore, the estimation error

$$\tilde{I}_d = I_d - \hat{I}_d = I_d - \frac{V_{dlc} - \hat{V}_{cd}}{R_d} \\ = I_d - \frac{V_{dlc} - (V_{cd} + \Delta)}{R_d} = \frac{\Delta}{R_d} = \Delta_d$$

converges to a bounded region in finite time where Δ is the combined effect of uncertainties in the estimation of \hat{V}_{cd} .

Now, under the condition $\hat{I}_d \rightarrow I_d - \Delta_d$ and considering (48), I_f can be reconstructed as $\hat{I}_f = I_{dlc} - \hat{I}_d = I_f + \Delta_d$. Therefore, we can write that

$$V_{dlc} - \hat{I}_f \hat{R}_f - \hat{V}_{cf} \rightarrow \tilde{V}_{cf} + \eta_{\text{comb2}} \quad (63)$$

where η_{comb2} is the combined effect of the uncertainties in the estimated quantities \hat{I}_f and \hat{R}_f . Subsequently, from (55), *Observer VI* can be written as

$$\dot{\tilde{V}}_{cf} = L_V \text{sgn}(\tilde{V}_{cf} + \eta_{\text{comb2}}). \quad (64)$$

Subtracting (64) from (46), the error dynamics for *Observer VI* can be written as

$$\dot{\tilde{V}}_{cf} = \frac{I_f}{C_f} + \eta_f - L_V \text{sgn}(\tilde{V}_{cf} + \eta_{\text{comb2}}). \quad (65)$$

Now, analyzing the error dynamics (65) via Lyapunov function candidate $V_V = 0.5s_{Vf}^2$, we can conclude that the sliding manifold $s_{Vf} = \tilde{V}_{cf} + \eta_{\text{comb2}} = 0$ can be achieved asymptotically. At the sliding manifold, we have $s_{Vf} = \tilde{V}_{cf} + \eta_{\text{comb2}} = 0$ and $\dot{s}_{Vf} = \dot{\tilde{V}}_{cf} + \dot{\eta}_{\text{comb2}} = 0$ and (65) can be written as

$$-\dot{\eta}_{\text{comb2}} = \frac{I_f}{C_f} + \eta_f - v_V \quad (66)$$

where v_V is the equivalent output error injection. Furthermore, considering (56) and (66), and considering $\hat{I}_f \rightarrow I_f$, the

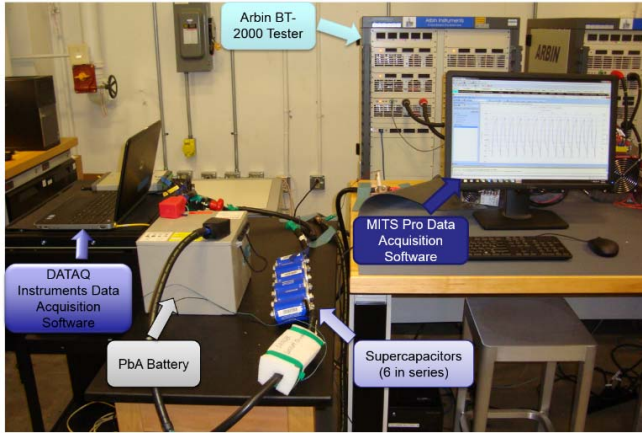


Fig. 5. Experimental test setup at the BACH Laboratory, CU-ICAR.

following can be written:

$$\begin{aligned} \frac{1}{\hat{C}_f} &= \frac{v_V}{\hat{I}_f} = \frac{\left(\frac{I_f}{C_f} + \eta_f + \dot{\eta}_{\text{comb}2}\right)}{I_f} \\ \Rightarrow \frac{1}{\hat{C}_f} &= \frac{1}{C_f} - \frac{(\eta_f + \dot{\eta}_{\text{comb}2})}{I_f}. \end{aligned} \quad (67)$$

Defining $C_{f-\text{inv}} = 1/C_f$, $\hat{C}_{f-\text{inv}} = 1/\hat{C}_f$, and $\tilde{C}_{f-\text{inv}} = C_{f-\text{inv}} - \hat{C}_{f-\text{inv}}$, we can write

$$\tilde{C}_{f-\text{inv}} = \frac{(\eta_f + \dot{\eta}_{\text{comb}2})}{I_f}. \quad (68)$$


Therefore, it can be concluded that the estimation error $\tilde{C}_{f-\text{inv}}$ converges to a bounded region determined by (68), in finite time. This follows the convergence of \tilde{C}_f to a bounded region in finite time. \square

Remark 8: Note that the parameters in both estimation schemes lose their identifiability when the current goes to zero. Therefore, parameters must be updated when the current value is nonzero and sufficiently high. When this is not satisfied, the estimates should be held at the last updated values. Owing to this, the parameter estimates are updated in longer periodic intervals and when the current values are sufficiently high.

IV. EXPERIMENTAL MODEL IDENTIFICATION AND VALIDATION: BATTERY AND DLC

In this section, we discuss the experimental test setup and the current profiles used to determine the characteristics of the PbA battery, the Maxwell BCAP1500 P270 DLC, and the HESS developed by connecting the PbA battery system in parallel with a module of six (6) DLCs connected in series. The experiments were conducted in the Battery Aging and Characterization (BACH) Laboratory at the Automotive Engineering Department, Clemson University. The HESS experimental setup is shown in Fig. 5. The experimental equipment consists of an Arbin BT-2000 testing station incorporating a programmable power supply and an electronic load, and capable of performing charge–discharge cycles with high precision and fast data acquisition (up to a rate of 100 Hz); an MITS Pro data acquisition software used to design test

TABLE I
PbA BATTERY SPECIFICATIONS

ARMASAFE™ PLUS; HASP-FT/6TAGM		
	Nominal Voltage	12 V
	Nominal Capacity C ₂₀	120 Ah
	Cold Cranking Amp	1225 A
	Temperature Range	-40°C to +80°C
	Cycle life at 20% DoD (depth of discharge)	3,500 cycles

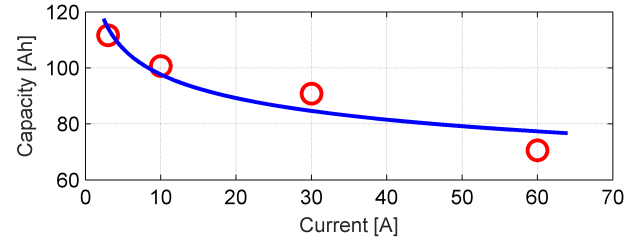


Fig. 6. PbA battery Peukert curve.

cycle profiles and control the Arbin tester, as well as real-time data review and analysis; DATAQ Instruments data acquisition software capable of fast and accurate data acquisition, while operating synchronously with the MITS Pro software; and a current shunt in order to measure the DLC current during the HESS experiments.

The following signals were measured: battery current I_{batt} , DLC current I_{dlc} , overall HESS current I_{total} , HESS voltage (which is same as V_{batt} and V_{dlc}), surface temperature of the battery T_{batt} , and surface temperature of the DLC T_{dlc} . Sections IV-A–IV-C discuss the identification of the parameters for the PbA battery model, the DLC model, and the HESS model.

A. PbA Battery Model Identification

The technical specifications of the 12 V, 120-Ah Armasafe Plus HASP-FT/6TAGM PbA battery are summarized in Table I, and further information can be obtained from [34]. All tests performed to understand the behavior of the battery and identify its model parameters were performed at ambient temperature of $23 \text{ }^\circ\text{C} \pm 0.2 \text{ }^\circ\text{C}$. Capacity tests were conducted at different current rates, and prior to each capacity test; the battery was fully charged and allowed to rest for a period of 8 h.

The Peukert curve for the PbA battery was determined on the basis of the results of the capacity tests in discharge, and is schematically represented in Fig. 6.

A pulse characterization test was specifically designed to characterize the dynamic performance of the PbA battery and identify its electrical parameters. Prior to the test, the battery was fully charged and allowed to rest for 8 h. The battery was then discharged from 100% SOC to 20% SOC, with discharging and charging pulse events performed at every 10% SOC discharge variation, i.e., at 100% SOC and 90% SOC. The current profile for the pulse discharge test is shown

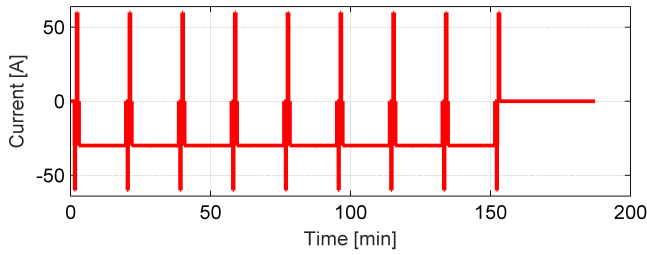


Fig. 7. PbA battery pulse characterization test current profile.

TABLE II
IDENTIFIED PbA BATTERY PARAMETERS

SOC (-)	R_{c^*} (Ω)	R_{d^*} (Ω)	R_{0,c^*} (Ω)	R_{0,d^*} (Ω)	C_{0,c^*} (F)	C_{0,d^*} (F)
100 %	0.0600	0.0023	0.0080	0.0046	730	1300
90 %	0.0070	0.0060	0.0060	0.0035	1000	1714
80 %	0.0062	0.0055	0.0055	0.0032	1054	1875
70 %	0.0056	0.0049	0.0051	0.0025	1137	2160
60 %	0.0056	0.0053	0.0050	0.0027	1200	2222
50 %	0.0062	0.0050	0.0048	0.0022	1250	2636
40 %	0.0062	0.0057	0.0042	0.0023	1381	2435
30 %	0.0049	0.0053	0.0045	0.0023	1333	2435
20 %	0.0070	0.0068	0.0048	0.0022	1917	2636

in Fig. 7. A total of six (6) parameters were identified, namely,

$$\theta_{\text{Batt}} = [R_{c^*}, R_{d^*}, R_{0,c^*}, R_{0,d^*}, C_{0,c^*}, C_{0,d^*}]^T.$$

Subscripts c^* and d^* , respectively, correspond to values identified during charging and discharging pulse events.

The open-circuit voltage (OCV) of the PbA battery E_0 was determined by performing a 0.025 C-rate discharge. This discharge rate is low enough to make the approximation of measured V_{batt} with E_0 reasonable. The battery dynamics were represented using a first-order electrical model. The initial estimates for the model parameters were determined at incremental battery SOC levels using graphical method. The parameter values were then identified through an optimization-based identification routine [36] with the objective to minimize the root-mean-square (rms) error between the experimental data and simulated voltage response signals. The final rms error resulting from this paper was 0.0565 V. Fig. 8 schematically represents the result of this parameter identification study.

The identified PbA battery parameter values are summarized in Table II.

B. DLC Model Identification

The technical specifications of the 2.70-V, 1500-F BCAP1500 DLCs used in this paper are summarized in Table III, and further information can be obtained from [35]. The DLC model parameters were identified using data obtained from the HESS experiments. Similar to the PbA battery, the optimal DLC electrical model parameters were obtained by minimizing the rms error between the experimental and simulated voltage response. The same approach was implemented to identify the DLC thermal model parameters.

TABLE III
DLC SPECIFICATIONS

Maxwell BCAP1500 P270 Ultracapacitor	
Rated Capacitance	1,500 F
Rated Voltage	2.70 V
Equivalent Series Resistance	0.47 m Ω
Maximum Peak Current	1150 A
Operating Temperature	-40°C to +65°C
Projected Cycle Life	10 ⁶ Cycles
Energy Density	5.4 Wh/kg
Power Density	6,600 W/kg

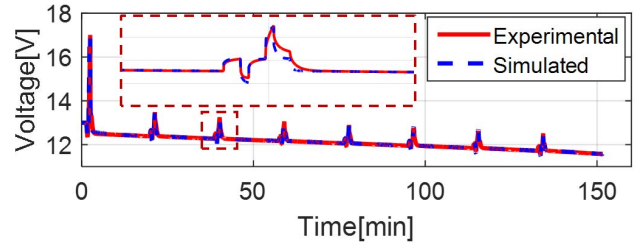


Fig. 8. Comparison of model and experimental voltage of the PbA battery.

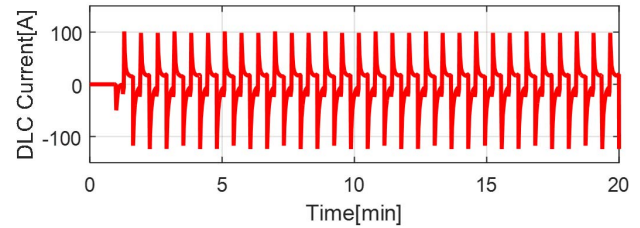


Fig. 9. Measured DLC current during the HESS experiment.

Fig. 9 presents the DLC current profile, and Fig. 10 compares the experimentally measured DLC voltage with the model-predicted voltage response. The final rms error resulting from this identification study was 0.0738 V. The final vector of identified parameters of the DLC model is

$$\begin{aligned} \theta_{\text{DLC}} &= [R_f, R_d, C_f, C_d, mc_{\text{dlc}}, hA_{\text{dlc}}]^T \\ &= [0.0008165, 1.35, 1408.29, 109.74, 852.33, 0.32]^T. \end{aligned}$$

C. HESS Model

The HESS is developed by combining the PbA battery in parallel with a module of six (6) supercapacitors connected in series with one another. While a new and fully charged PbA battery has an OCV of 13 V, the fully charged DLC series system has an overall voltage of 16.2 V. Prior to combining the PbA battery with the DLC system, the PbA battery was

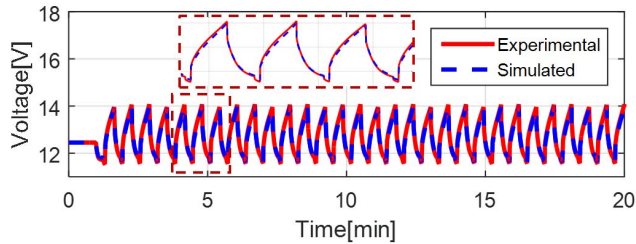


Fig. 10. Comparison of experimental and simulated DLC voltage.

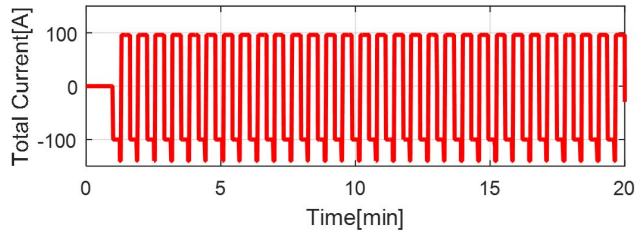


Fig. 11. Start and stop experimental current profile used for the HESS.

discharged to 90% SOC and the DLC system voltage was set to 100 mV lower than the OCV of the PbA battery at 90% SOC. This is done in order to ensure safe and reliable operation of the DLC system by preventing an over-voltage situation with respect to the battery.

The HESS model is developed by combining the electrical models and thermal models of the PbA battery and DLC systems. The current profile implemented to simulate the start and stop technology application is presented in Fig. 14. Electrical and thermal parameters were identified for the PbA battery using current, voltage, and temperature measurements from the HESS experiments.

The start and stop current profile used to excite the HESS in Fig. 11 consisted of 30 repetitions of the following cycle:

- Step 1: 60 s of discharge at 45 A;
- Step 2: 3 s of discharge at 100 A;
- Step 3: 60 s of charge at 50 A.

Step 1 is a representation of the current from the battery during nominal operation; Step 2 represents the peak cranking current required to start the engine; and Step 3 represents the current supplied back to the battery to bring it back to its SOC at the initial stage of the cycle. The comparison of the experimental and simulated HESS voltage is shown in Fig. 12. The vector of electrical and thermal parameter values used in the HESS model is: $\theta_{\text{HESS}} = [R_f, R_d, C_f, C_d, mc_{\text{dlc}}, hA_{\text{dlc}}, \dots$

$$\begin{aligned} & R_{c^*}, R_{d^*}, R_{0,c^*}, R_{0,d^*}, C_{0,c^*}, C_{0,d^*}, mc_{\text{batt}}, hA_{\text{batt}}]^T \\ &= [0.0008165, 1.35, 1408.29, 109.74, 852.33, 0.32, \dots \\ & \quad 0.0071, 0.0060, 0.0263, 0.0053, 1294.9, 3201.5, \\ & \quad 62430, 19.89]^T. \end{aligned}$$

The rms error between the experimental and the HESS model-predicted voltage response is 0.0357 V. Section V presents the validation of a novel estimation scheme using the HESS electrical–thermal model developed in this section.

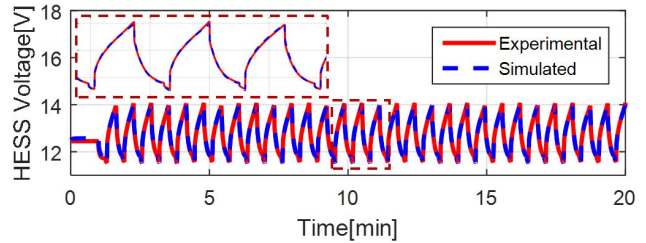


Fig. 12. Comparison of experimental and simulated HESS voltage response for the optimized parameters at 90% SOC.

V. ESTIMATION SCHEME VALIDATION

In this section, we validate the effectiveness of the proposed estimation scheme. First, we evaluate the performance of the scheme using simulation studies, where the observers use the “outputs” from the simulation “plant model.” This scenario indicates ideal conditions with no modeling and measurement uncertainties. Next, we evaluate the performance of the scheme using the experimental data, where the observers use the “outputs” from the experimental data which captures the modeling and measurement uncertainties. Note that, unlike “minutes” in the model identification section, we report the convergence times of the estimated variables in seconds as they are easier to view in that time scale.

A. Validation Using Simulation Data

In this section, the effectiveness of the proposed estimation scheme is evaluated via simulation studies. The HESS plant model is implemented in MATLAB/Simulink platform with the parameters identified in Section IV. The current profile applied to HESS and individual battery and DLC current responses are shown in Fig. 13. Furthermore, Fig. 13 also shows the HESS voltage response from the model, and battery and DLC temperature responses from the model. The *Observer I* and *Observer IV*, which are based on the temperature dynamics, are initialized with correct initial temperature as we assume the temperature measurements are available. The other observers in the estimation scheme are initialized with different initial conditions than the HESS plant to evaluate the convergence of the estimated variables. Furthermore, a zero mean white Gaussian noise with 5 mV and 0.3 °C standard deviation is added to the measured voltages and temperatures, respectively. Fig. 14 illustrates the estimation performance on the DLC variables. As can be seen from Fig. 14, the estimation scheme is able to estimate the internal resistance and capacitance, and the internal voltage across the capacitance with sufficient accuracy. The estimates of the internal resistance, capacitance, and internal voltage converge to the actual value within 530, 650, and 4 s. Fig. 15 shows the estimation performance on the battery variables. Similar to the DLC variables, the estimation scheme is able to estimate the battery internal resistance, capacity, and SOC with reasonable accuracy. The estimates of the internal resistance, capacity, and SOC converge to their true value within 250, 2000, and 300 s, respectively.

Remark 9: As analyzed in [33], capacity estimation accuracy depends on three factors: 1) the slope of the OCV versus

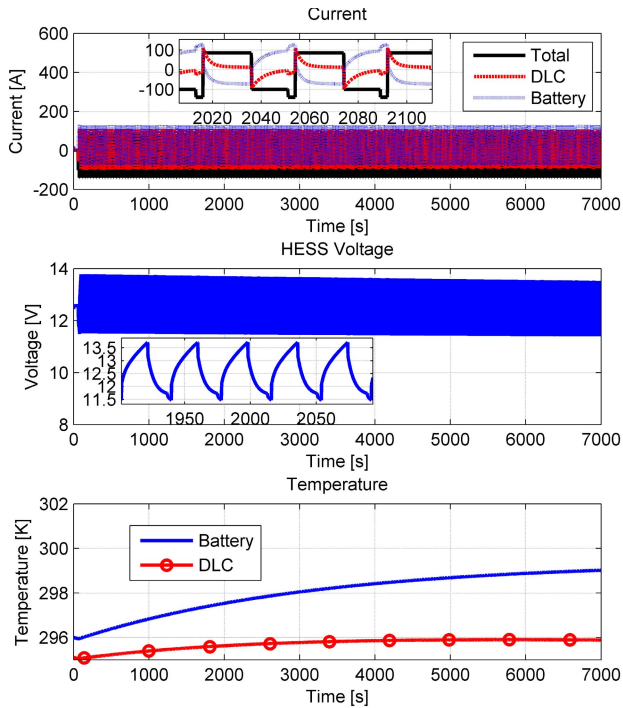


Fig. 13. Applied total current to HESS (black solid line), individual battery model and DLC model current and temperature models response, and corresponding HESS model voltage response.

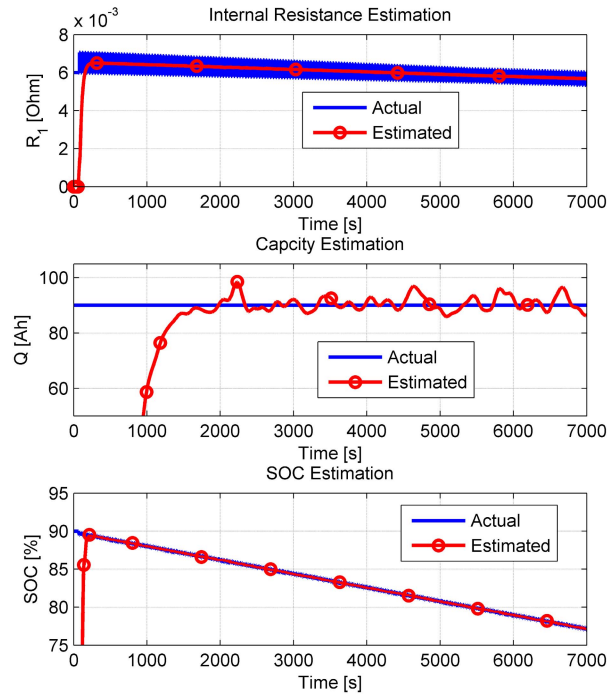


Fig. 15. Actual and estimated variables of PbA battery. “Actual” denotes the parameter values in the model, and “estimated” denotes the variables estimated by the proposed estimation scheme when the model output (and not the experimental measured output) is fed to the observer.

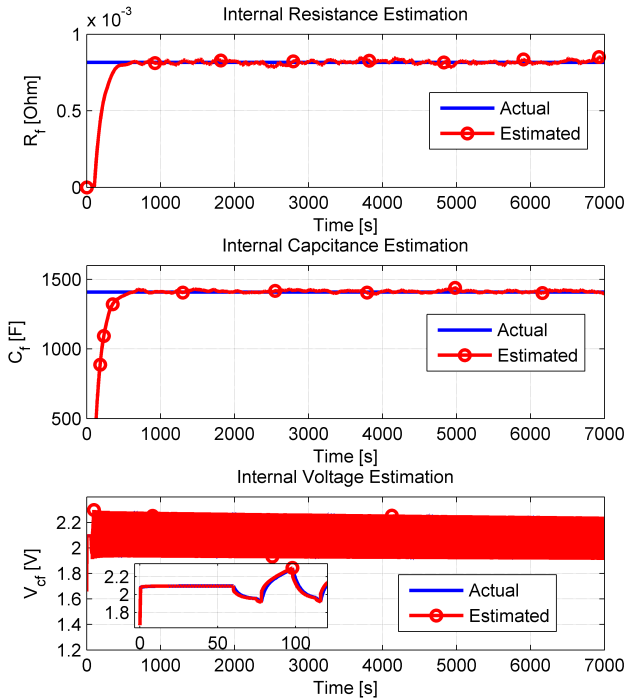


Fig. 14. Actual and estimated variables of DLC. “Actual” denotes the parameter values in the model, and “estimated” denotes the variable estimated by the proposed estimation scheme when the model output (and not the experimental measured output) is fed to the observer.

SOC curve; 2) the length of SOC swing; and 3) the level (mean and variance) of the voltage measurement noise. The PbA battery used in this paper has a steeper slope in the 10%–90% SOC region than that of lithium iron phosphate

and lithium nickel manganese cobalt oxide Li-ion chemistries discussed in [33]. Furthermore, a 5-mV standard deviation in voltage measurement noise was assumed as opposed to the 10-mV standard deviation used in [33]. Because of these factors, the capacity estimation in our case has converged to its real value within 5% of SOC swing. In summary, steeper OCV–SOC curve and lesser standard deviation of measurement noise enable capacity estimation to converge within a smaller SOC swing.

B. Validation Using Experimental Data

In this section, the effectiveness of the proposed estimation scheme is evaluated using the experimental data. The current profile applied to HESS and individual battery and DLC current responses are shown in Fig. 16. Furthermore, Fig. 16 also shows the experimental HESS voltage response, and the experimental battery and DLC temperature responses. The experimental voltage, current, and temperature are fed to the observers as feedback signals in the estimation scheme.

Fig. 17 illustrates the estimation performance regarding the DLC variables. As can be seen from Fig. 17, the estimation scheme is able to estimate the internal resistance and capacitance, and the internal voltage across the capacitance with reasonable accuracy. The estimates of the internal resistance, capacitance, and internal voltage converge to the actual value within 550, 570, and 400 s. The steady-state errors in estimation of the internal resistance, capacitance, and internal voltage stay within the 20%, 10%, and 40-mV band. Note that the internal resistance estimation error is quite high. This performance degradation can be attributed to two possible

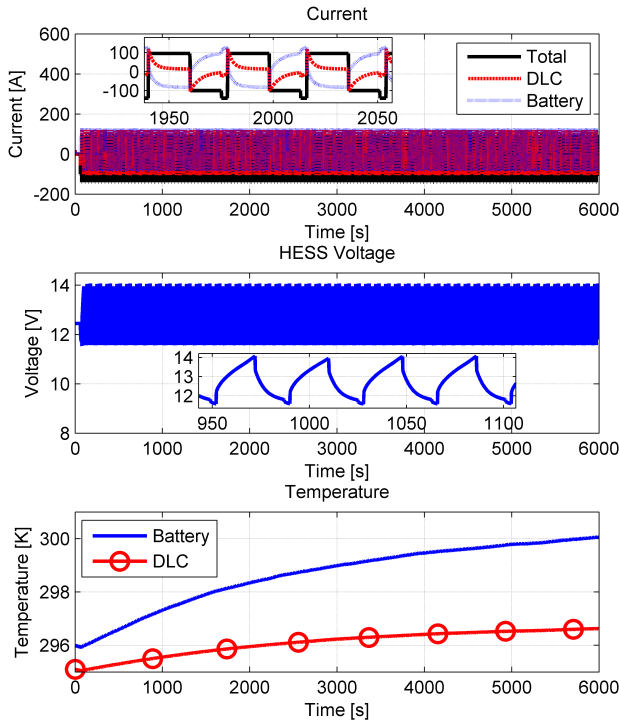


Fig. 16. Applied total current to HESS (black solid line), individual experimental battery and DLC current and experimental temperature response, and corresponding measured HESS voltage response.

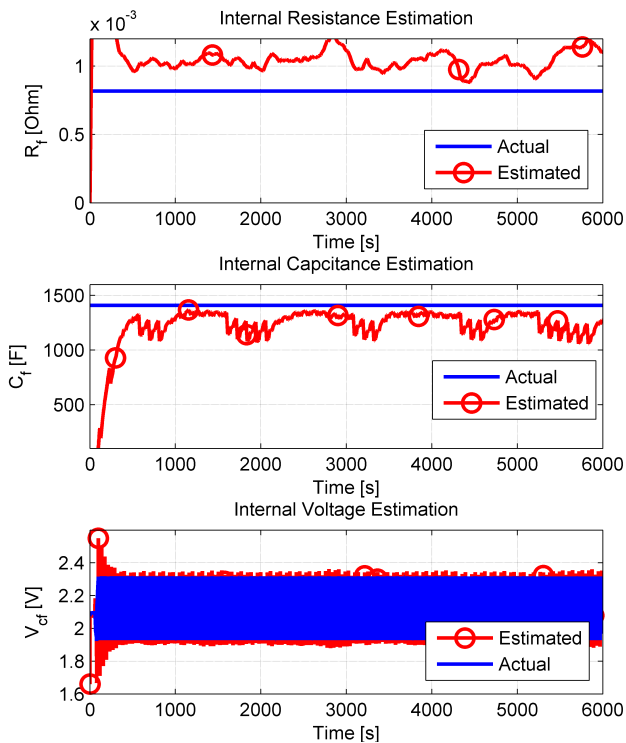


Fig. 17. Actual and estimated variables of DLC. “Actual” denotes the parameter values in the model, and “estimated” denotes the variable estimated by the proposed estimation scheme when experimental data are used to feed the observer.

issues: 1) the sensitivity of the sliding mode to sensor inaccuracies and 2) the uncertainties in the DLC thermal model. As the DLC thermal model is utilized to estimate

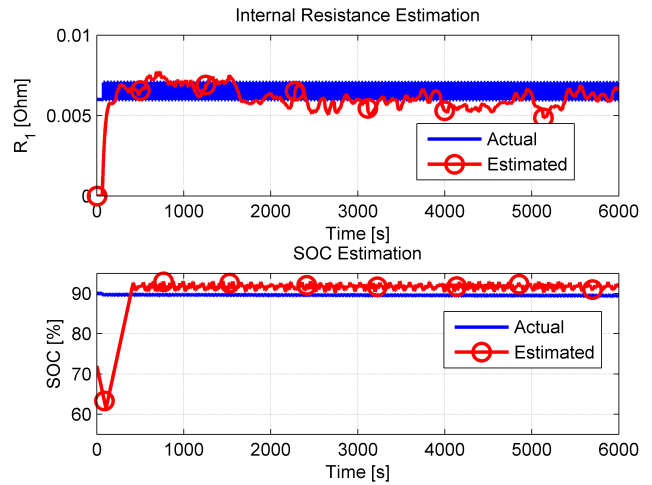


Fig. 18. Actual and estimated variables of DLC. “Actual” denotes the parameter values in the model, and “estimated” denotes the variable estimated by the proposed estimation scheme when experimental data are used to feed the observer.

DLC internal resistance, the estimate is corrupted by thermal model uncertainties, as shown after (61) where the uncertainty is denoted by the term η_{T_D} . This particular result points out one of the limitations of the proposed scheme. As future extension of the scheme, further investigations are necessary in order to reduce the effect of such uncertainties and sensor noise. Fig. 18 shows the estimation performance regarding the battery variables. Similar to the DLC variables, the estimation scheme is able to estimate the battery internal resistance, capacity, and SOC with reasonable accuracy. The estimates of the internal resistance and SOC converge to their true values within 220 and 380 s, respectively. The steady-state errors in estimating the internal resistance and SOC stay within the 10% and 2% band.

Remark 10: Note that for the battery, the capacity could not be estimated. This is due to the particular current profile chosen, for which the SOC stays almost constant. (From Fig. 18, one can see that SOC is approximately constant around 90%). As the SOC does not change, the dynamic equation of the SOC becomes $0 = -(I_{\text{batt}}/Q)$ (with $\text{SOC} = 0$). Therefore, it was not possible to reconstruct the capacity Q using this equation. Essentially, there is not enough/persistent excitation in the SOC dynamics which affects the estimation capability of the scheme. In contrast, the SOC in the simulation studies is not constant, and the SOC swing is 90%–77% during the simulation time (as shown in Fig. 15). This SOC swing provides sufficient excitation in SOC dynamics, and hence the proposed scheme was able to estimate capacity accurately. This confirms the previous finding in [33] that accurate capacity estimation is only possible under sufficient SOC swing.

VI. CONCLUSION

In this paper, a multiobserver-based estimation scheme is presented for combined state and parameter estimation of battery-DLC HESS. The scheme consists of two separate battery and DLC state-parameter estimators based on the

sliding mode methods. Each estimator consists of a cascaded observer-based structure that utilizes the coupled electrical–thermal dynamics of battery and DLC. The effectiveness of the scheme is tested via simulation and experimental studies. In the experimental studies, the steady-state estimation errors of the DLC internal resistance, capacitance, and internal voltage stays within the 20%, 10%, and 40-mV band. For the battery, steady-state estimation errors of the internal resistance and SOC stay within the 10% and 2% band.

We conclude this paper with the following remarks.

- 1) The scheme exploits the battery/DLC electrical–thermal coupling to decompose the overall estimation problem into two coupled subproblems. This framework can be extended to other applications with coupled systems.
- 2) A limitation of the proposed scheme is that the performance degrades under high level of voltage measurement noise and thermal model uncertainty. One potential option to mitigate the effect of thermal model uncertainty is to utilize a more accurate thermal model, e.g., two-state thermal model in [23].
- 3) The identifiability of the parameters depends on sufficient excitation of current input to the battery and DLC, which is in line with [33]. Specifically, sufficient SOC swing is necessary for successful capacity estimation.
- 4) Finally, future extensions of the scheme could include the following studies:
 - a) extension to nonlinear battery and DLC models where the model parameters depend on the system states, e.g., temperature and SOC;
 - b) robustness with respect to voltage measurement noise.

REFERENCES

- [1] C.-J. Chiang, J.-L. Yang, and W.-C. Cheng, “EKF-based estimation of SOC and temperature in ultracapacitors,” in *Proc. IEEE Int. Conf. Control Autom.*, Jun. 2013, pp. 274–279.
- [2] P. Thounthong, S. Raël, and B. Davat, “Energy management of fuel cell/battery/supercapacitor hybrid power source for vehicle applications,” *J. Power Sour.*, vol. 193, no. 1, pp. 376–385, 2009.
- [3] P. Thounthong, V. Chunkag, P. Sethakul, S. Sikkabut, S. Pierfederici, and B. Davat, “Energy management of fuel cell/solar cell/supercapacitor hybrid power source,” *J. Power Sour.*, vol. 196, no. 1, pp. 313–324, 2011.
- [4] M. Richter, S. Zinser, M. Stiegeler, M. Mendes, and H. Kabza, “Energy management for range enlargement of a hybrid battery vehicle with battery and double layer capacitors,” in *Proc. 14th Eur. Conf. Power Electron. Appl.*, 2011, pp. 1–6.
- [5] S. J. Moura, N. A. Chaturvedi, and M. Krstic, “PDE estimation techniques for advanced battery management systems—Part I: SOC estimation,” in *Proc. Amer. Control Conf. (ACC)*, 2012, pp. 559–565.
- [6] D. Di Domenico, A. Stefanopoulou, and G. Fiengo, “Lithium-ion battery state of charge and critical surface charge estimation using an electrochemical model-based extended Kalman filter,” *J. Dyn. Syst., Meas., Control*, vol. 132, no. 6, p. 061302, 2010.
- [7] S. Dey, B. Ayalew, and P. Pisu, “Nonlinear adaptive observer for a lithium-ion battery cell based on coupled electrochemical–thermal model,” *ASME J. Dyn. Syst., Meas., Control*, vol. 137, no. 11, p. 111005, 2015.
- [8] G. L. Plett, “Extended Kalman filtering for battery management systems of LiPB-based HEV battery packs: Part 3. State and parameter estimation,” *J. Power Sour.*, vol. 134, no. 2, pp. 277–292, 2004.
- [9] M. Rubagotti, S. Onori, and G. Rizzoni, “Automotive battery prognostics using dual extended Kalman filter,” in *Proc. ASME Dyn. Syst. Control Conf.*, 2009, pp. 257–263.
- [10] B. S. Bhangu, P. Bentley, D. A. Stone, and C. M. Bingham, “Nonlinear observers for predicting state-of-charge and state-of-health of lead-acid batteries for hybrid-electric vehicles,” *IEEE Trans. Veh. Technol.*, vol. 54, no. 3, pp. 783–794, May 2005.
- [11] I.-S. Kim, “A technique for estimating the state of health of lithium batteries through a dual-sliding-mode observer,” *IEEE Trans. Power Electron.*, vol. 25, no. 4, pp. 1013–1022, Apr. 2010.
- [12] C. Unterrieder, R. Prieuwater, S. Marsili, and M. Huemer, “Battery state estimation using mixed Kalman/hinfinity, adaptive Luenberger and sliding mode observer,” in *Proc. IEEE Veh. Power Propuls. Conf. (VPPC)*, Oct. 2013, pp. 71–76.
- [13] F. Zhang, G. Liu, and L. Fang, “A battery state of charge estimation method using sliding mode observer,” in *Proc. IEEE Conf. Intell. Control Autom.*, Jun. 2008, pp. 989–994.
- [14] A. Belhani, N. K. M’Sirdi, and A. Naamane, “Adaptive sliding mode observer for estimation of state of charge,” *Energy Procedia*, vol. 42, pp. 377–386, 2013. [Online]. Available: <https://doi.org/10.1016/j.egypro.2013.11.038>
- [15] Y. Hu and S. Yurkovich, “Battery cell state-of-charge estimation using linear parameter varying system techniques,” *J. Power Sour.*, vol. 198, pp. 338–350, Jan. 2012.
- [16] O. Bohlen, J. Kowal, and D. U. Sauer, “Ageing behaviour of electrochemical double layer capacitors: Part II. Lifetime simulation model for dynamic applications,” *J. Power Sour.*, vol. 173, no. 1, pp. 626–632, 2007.
- [17] C.-J. Chiang, J.-L. Yang, and W.-C. Cheng, “Dynamic modeling of the electrical and thermal behavior of ultracapacitors,” in *Proc. 10th IEEE Int. Conf. Control Autom.*, Jun. 2013, pp. 1839–1844.
- [18] D. Pavković, V. Smetko, M. Hrgetić, and A. Komljenović, “Dual Kalman filter-based SOC/SOH estimator for an ultracapacitor module,” in *Proc. IEEE Conf. Control Appl.*, Oct. 2014, pp. 1783–1788.
- [19] A. Hammar, P. Venet, R. Lallemand, G. Coquery, and G. Rojat, “Study of accelerated aging of supercapacitors for transport applications,” *IEEE Trans. Ind. Electron.*, vol. 57, no. 12, pp. 3972–3979, Dec. 2010.
- [20] A. Nadeau, G. Sharma, and T. Soyata, “State-of-charge estimation for supercapacitors: A Kalman filtering formulation,” in *Proc. IEEE Int. Conf. Acoust., Speech Signal Process.*, May 2014, pp. 2194–2198.
- [21] M. Pucci, G. Vitale, G. Cirrincione, and M. Cirrincione, “Parameter identification of a double-layer-capacitor 2-branch model by a least-squares method,” in *Proc. IEEE IECON*, Nov. 2013, pp. 6770–6776.
- [22] A. Eddahech, O. Briat, M. Ayadi, and J.-M. Vinassa, “Ultracapacitor performance determination using dynamic model parameter identification,” in *Proc. IEEE Int. Symp. Ind. Electron.*, May 2013, pp. 1–5.
- [23] Y. Parvini, J. B. Siegel, A. G. Stefanopoulou, and A. Vahidi, “Supercapacitor electrical and thermal modeling, identification, and validation for a wide range of temperature and power applications,” *IEEE Trans. Ind. Electron.*, vol. 63, no. 3, pp. 1574–1585, Mar. 2016.
- [24] S. Dey, S. Mohon, P. Pisu, B. Ayalew, and S. Onori, “Online state and parameter estimation of battery-double layer capacitor hybrid energy storage system,” in *Proc. IEEE Conf. Decision Control*, Dec. 2015, pp. 676–681.
- [25] V. Utkin, J. Guldner, and J. Shi, *Sliding Mode Control in Electro-Mechanical Systems*. Boca Raton, FL, USA: CRC Press, 1999.
- [26] S. Fiorenti, J. Guanetti, Y. Guezennec, and S. Onori, “Modeling and experimental validation of a hybridized energy storage system for automotive applications,” *J. Power Sour.*, vol. 241, pp. 112–120, Nov. 2013.
- [27] R. Mahamud and C. Park, “Reciprocating air flow for Li-ion battery thermal management to improve temperature uniformity,” *J. Power Sour.*, vol. 196, pp. 5685–5696, Jul. 2011.
- [28] J. Marcicki, S. Onori, and G. Rizzoni, “Nonlinear fault detection and isolation for a lithium-ion battery management system,” in *Proc. ASME Dyn. Syst. Control Conf.*, 2010, pp. 607–614.
- [29] R. Feng, S. Zhao, and X. Lu, “On-line estimation of dynamic state-of-charge for lead acid battery based on fuzzy logic,” in *Proc. 2nd Int. Conf. Meas., Inf. Control*, 2013, pp. 447–451.
- [30] F. Baronti, N. Femia, R. Saletti, and W. Zamboni, “Comparing open-circuit voltage hysteresis models for lithium-iron-phosphate batteries,” in *Proc. 40th Annu. Conf. IEEE Ind. Electron. Soc.*, Oct./Nov. 2014, pp. 5635–5640.
- [31] Z. Chen, S. Qiu, M. A. Masrur, and Y. L. Murphey, “Battery state of charge estimation based on a combined model of extended Kalman filter and neural networks,” in *Proc. Int. Joint Conf. Neural Netw.*, 2011, pp. 2156–2163.
- [32] R. Ahmed *et al.*, “Model-based parameter identification of healthy and aged Li-ion batteries for electric vehicle applications,” SAE Tech. Paper 2015-01-0252, 2015.

- [33] X. Lin and A. G. Stefanopoulou, "Analytic bound on accuracy of battery state and parameter estimation," *J. Electrochem. Soc.*, vol. 162, no. 9, pp. A1879–A1891, 2015.
- [34] Hawkeraplus. (2012). *HASP-FT/6TAGM*. Accessed: Feb. 1, 2015. [Online]. Available: http://www.hawkeraplus.com/pdf/battery-data-sheets/WEB_Energys_ArmaSafe_Plus_1HASP-FT-6TAGM_Jan-2012_V01_EN.pdf
- [35] Maxwell. (2014). *Datasheet K2 Ultracapacitors—2.7 V Series*. Accessed: Feb. 1, 2015. [Online]. Available: http://www.maxwell.com/images/documents/K2Series_DS_1015370_5_20141104.pdf
- [36] C. R. Houck, J. A. Joines, and M. G. Kay, "A genetic algorithm for function optimization: A MATLAB implementation," in *Proc. Cite-seer*, 1996, pp. 1–14. Accessed: Feb. 8, 2015. [Online]. Available: <http://citeseerx.ist.psu.edu/viewdoc/summary?doi=10.1.1.22.4413>



Satadru Dey (S'13–M'15) received the master's degree in control systems from IIT Kharagpur, Kharagpur, India, in 2010, and the Ph.D. degree in automotive engineering from Clemson University, Clemson, SC, USA, in 2015.

From 2010 to 2012, he was a Control Engineer with General Electric Company, Hyderabad, India. He was a Post-Doctoral Researcher with the University of California, Berkeley, CA, USA, from 2015 to 2017. He is currently an Assistant Professor of electrical engineering with the University of Colorado,

Denver, CO, USA. His technical background is in the area of controls. His current research interests include energy and transportation systems, developing controls, estimation and diagnostic algorithms for batteries, ultracapacitors, fuel cells, electric vehicles, and connected and autonomous vehicles.



Sara Mohon (M'15) received the B.S. degree in physics from the College of William and Mary, Williamsburg, VA, USA, in 2009, and the M.S. and Ph.D. degrees in automotive engineering from Clemson University, Clemson, SC, USA, in 2012 and 2015, respectively.

She is currently an Electrified Powertrain Engineer with BorgWarner, Auburn Hills, MI, USA. She is with the Hybrid and Electrical Systems Team, the Corporate Advanced Engineering Department, Auburn Hills. She is involved in building hybrid

supervisory controllers for simulations and demonstration vehicles. She has authored or co-authored several publications in reputable international technical journals and conference proceedings. Her current research interests include modelings, controls, diagnostics, and prognostics for electric vehicles and their components.



Beshah Ayalew (M'06) received the M.S. and Ph.D. degrees in mechanical engineering from Penn State University, State College, PA, USA, in 2000 and 2005, respectively.

He is currently a Professor of automotive engineering and the Director of the DOE GATE Center of Excellence in Sustainable Vehicle Systems, Clemson University, Clemson, SC, USA. His current research interests include systems dynamics and controls.

Dr. Ayalew is an Active Member of ASME's Vehicle Design Committee, IEEE's Control Systems Society, and SAE. He was a recipient of the Ralph Teeter Educational Award from SAE in 2014, the Clemson University Board of Trustees Award for Faculty Excellence in 2012, the NSF CAREER Award in 2011, and the Penn State Alumni Association Dissertation Award in 2005.



Harikesh Arunachalam (S'14) received the B.E. degree in mechanical engineering from the Birla Institute of Technology and Science, Pilani, India, in 2010, and the M.S. degree in mechanical engineering from the University of California, San Diego, CA, USA, in 2011. He is currently pursuing the Ph.D. degree with the Department of Automotive Engineering, Clemson University, Clemson, SC, USA.

His current research interests include multiscale electrochemical modelings, simulation, parameter identification, experimental validation of lithium-ion batteries, electrical–thermal modelings, system-level identification of PbA batteries and supercapacitors, and control-oriented modeling of the thermal and soot oxidation dynamics in engine exhaust after treatment systems such as gasoline particulate filters.

Mr. Arunachalam was a recipient of the Student Best Paper Award at the first IEEE Conference on Control Technology and Applications in 2017.



Simona Onori (SM'15) received the Laurea degree (*summa cum laude*) in computer science engineering from the University of Rome Tor Vergata, Rome, Italy, in 2003, the M.S. degree in electrical engineering from the University of New Mexico, Albuquerque, NM, USA, in 2004, and the Ph.D. degree in control engineering from the University of Rome Tor Vergata, in 2007.

In 2013, she joined the Clemson University–International Center for Automotive Research, Greenville, SC, USA, as an Assistant Professor,

where she also held a joint appointment with the Electrical and Computer Engineering Department. She held visiting professor positions at the University of Trento, Trento, Italy, in 2014; Beijing Institute of Technology, Beijing, China, 2015; and University of Orleans, Orleans, France, 2016. Since 2017, she has been an Assistant Professor with the Department of Energy Resources Engineering, Stanford University, Stanford, CA, USA.

Dr. Onori was a recipient of the 2017 NSF CAREER Award, the 2017 Clemson University College of Engineering and Science Dean's Faculty Fellows' Award, the 2017 Clemson University Esin Gulari Leadership and Service Award, the 2016 Energy Leadership Award in the category Emerging Leader (for the Carolinas), the 2015 Innovision Award, South Carolina, the 2012 Lumley Interdisciplinary Research Award, and the 2011 Outstanding Technology Team Award, TechColumbus. She is a PSG Distinguished Visiting Professor awarded by the Managing Trustee of PSG College of Technology, India, in 2017.